



VLASS Project Memo #11

Evaluation of primary beam correction, beam polarization, & TEC correction

Frank Schinzel (NRAO)

October 3, 2018

1 Introduction

This document summarizes verification work that was primarily performed evaluating the application of standard ionospheric correction using CASA for VLASS. In the course of this it was also possible to evaluate the quality of primary beam correction for single field imaging and the effect of a lack of full-polarization primary beam correction.

2 Datasets

Among all the VLASS1.1 datasets a small representative subset was chosen, sampling a wide range of ionospheric conditions. These can be broken into four categories and have the following properties:

1. high average total electron content (TEC) and high Δ TEC.
 - VLASS1.1.sb34346984.eb34356943.58004.0160307176
TEC = 20.15; Δ TEC = 19.14
17-Sep-08 00:23:24 (18:23 local) - 17-Sep-08 04:11:11 (22:11 local)
sunset into night: 19:23 local sunset
Flux calibrator: 3C286, phase calibrators are point sources
Calibrators in OTF fields: J1915+6548, J1933+6540, J1959+6508
 - VLASS1.1.sb34920826.eb35001824.58155.24291935185
TEC = 23.15; Δ TEC = 16.00
18-Feb-06 05:50:10 (22:50 local) - 18-Feb-06 13:28:09 (06:28 local)
into sunset
Flux calibrator 3C286, structure of phase calibrators unknown
Calibrators in OTF field: A0837-3409, J1257-3155

2. low average TEC and high Δ TEC.

- VLASS1.1.sb34476823.eb34548285.58025.047613229166
TEC = 10.81; Δ TEC = 29.96
17-Sep-29 01:08:35 (19:08 local) - 17-Sep-29 09:02:36 (03:02 local)
sunset at 18:52 local
Flux calibrator 3C286, phase calibrators are point sources
Calibrators in OTF fields: J2025+0316, A2023-0123, J0022+0014, T0032+0136,
J0040+0125, C0029-0113, T0014-0205, C0030-0211

3. low average TEC and low Δ TEC.

- VLASS1.1.sb34667861.eb34684334.58067.0700902199
TEC = 7.37; Δ TEC = 1.88
17-Nov-10 01:42:48 (18:42 local) - 17-Nov-10 08:58:49 (01:58 local)
sunset at 17:04
Flux calibrator 3C48, structure of phase calibrators unknown
Calibrators in OTF fields: J0157+7442, J0019+7327, J0747+7639, J0626+8202,
J0749+7420
- VLASS1.1.sb34422762.eb34486846.58018.47191952546
TEC = 11.42; Δ TEC = 8.11
17-Sep-22 11:19:35 (05:19 local) - 17-Sep-22 17:07:26 (11:07 local)
sunrise into day: sunrise at 6:54
Flux calibrator 3C48, phase calibrators are point sources
Calibrators in OTF fields: J0737+6430, J0756+6347, J0728+5701

The datasets were each calibrated twice, in one case the VLASS pipeline was executed with 'hifv_priorcal(tecmaps=True)' and in the other case with 'hifv_priorcal(tecmaps=False)'. Figures 1 – 5 give a visual representation of TEC changes across a given dataset. The TEC zenith values are obtained from the IONEX datasets available from NASA¹.

After this, single field, standard gridded, images were obtained for each field containing a bright calibrator source. In addition, in the case of VLASS1.1.sb34920826.eb35001824.58155.24291935185 a 10x1 square-degree stripe OTF mosaic was obtained. In the case of VLASS1.1.sb34667861.eb34684334.58067.0700902199, 1 square degree coarse cubes mosaics were generated for each of the calibrator fields in the dataset. The mosaics were produced by James Robnett, at the same time testing imaging pipeline processing.

¹<ftp://cdis.gsfc.nasa.gov/gnss/products/ionex/>

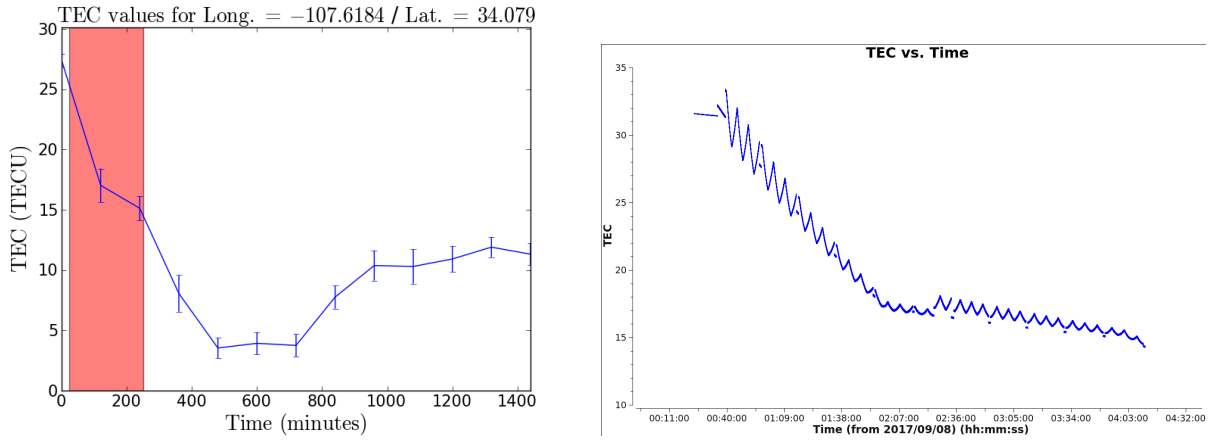


Figure 1: *Left:* Vertical (zenith) TEC vs time for VLASS1.1.sb34346984.eb34356943.58004.0160307176. The highlighted areas mark the duration of the observation. *Right:* Projected TEC vs time for all scans in VLASS1.1.sb34346984.eb34356943.58004.0160307176.

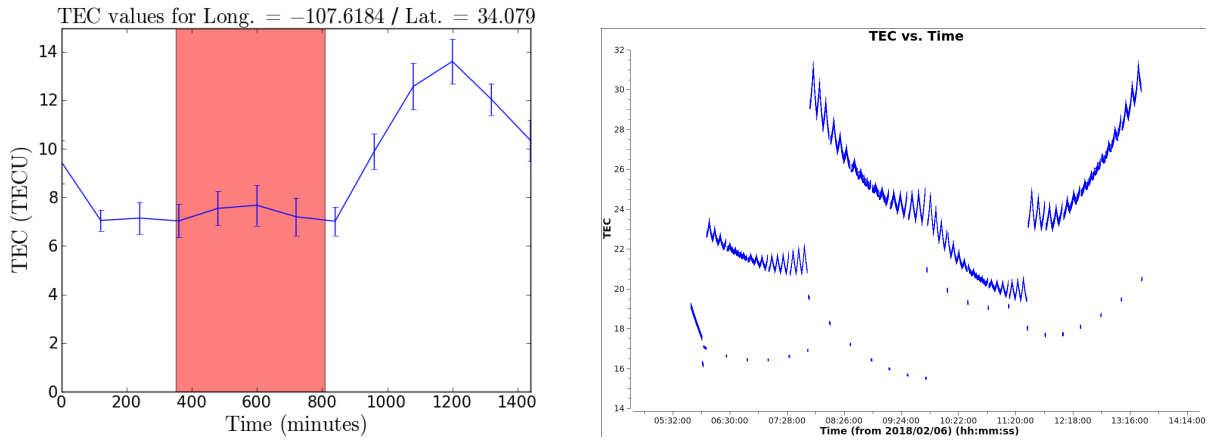


Figure 2: *Left:* Vertical (zenith) TEC vs time for VLASS1.1.sb34920826.eb35001824.58155.2429193518. The highlighted areas mark the duration of the observation. *Right:* Projected TEC vs time for all scans in VLASS1.1.sb34920826.eb35001824.58155.2429193518.

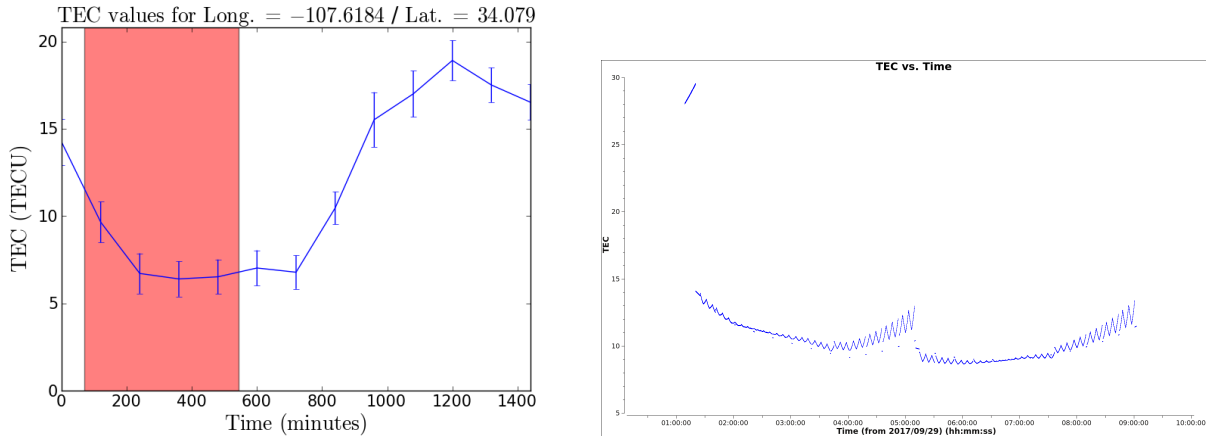


Figure 3: *Left:* Vertical (zenith) TEC vs time for VLASS1.1.sb34476823.eb34548285.58025.047613229166. The highlighted areas mark the duration of the observation. *Right:* Projected TEC vs time for all scans in VLASS1.1.sb34476823.eb34548285.58025.047613229166.

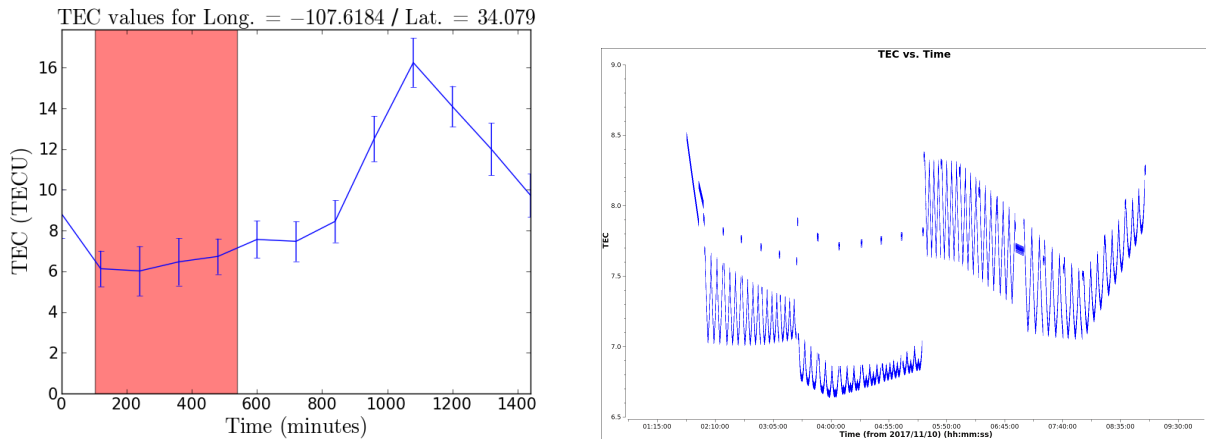


Figure 4: *Left:* Vertical (zenith) TEC vs time for VLASS1.1.sb34667861.eb34684334.58067.0700902199. The highlighted areas mark the duration of the observation. *Right:* Projected TEC vs time for all scans in VLASS1.1.sb34667861.eb34684334.58067.0700902199.

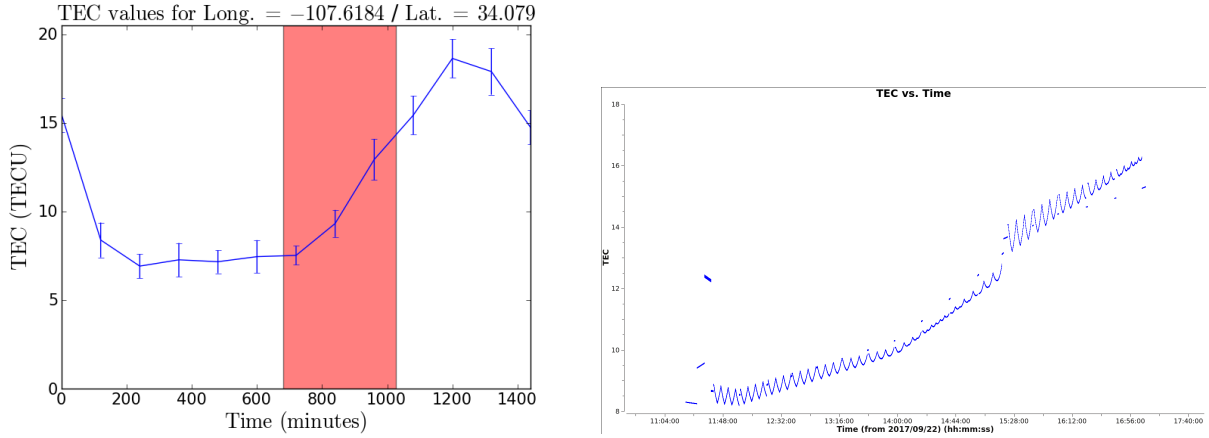


Figure 5: *Left:* Vertical (zenith) TEC vs time for VLASS1.1.sb34422762.eb34486846.58018.47191952546. The highlighted areas mark the duration of the observation. *Right:* Projected TEC vs time for all scans in VLASS1.1.sb34422762.eb34486846.58018.47191952546.

3 Results

3.1 Stokes-I primary beam correction

Single field images were made for all bright sources. Here we focus on J1915+6548² and J0019+7327³. Table 1 lists the imaged fields for each source and their on-sky separation from the primary beam center. Figure 6 shows the resulting amplitude ratios for a single spectral window, single polarization, after primary beam correction. These show that across an on-the-fly (OTF) scan row, where the two objects are imaged at different locations in the primary antenna beam, the residual flux densities after primary beam correction deviate by about $\pm 20\%$. Thus, affecting both flux density measurements and in particular spectral index values derived from OTF data. No deeper investigation was made into the effect of this primary beam error on mosaicked images. In most cases, the added error due to poor primary beam correction on flux densities derived from mosaics should mostly average out and only add a few percent of uncertainty depending on where the source passes through the primary beam, with the highest error expected from sources lying exactly in-between OTF rows.

Next, a possible offset between assumed delay/phase center and antenna pointing was investigated using the CASA task 'fixvis' to shift the phase center with respect to the delay center in right ascension (RA), effectively corresponding to a shift of the location of the center of the primary beam along the OTF scan direction axis. The phase center was shifted in fractions of half integration steps in RA from -2.0 integrations to +2.0

²VLASS1.1.sb34346984.eb34356943.58004.0160307176

³VLASS1.1.sb34667861.eb34684334.58067.0700902199

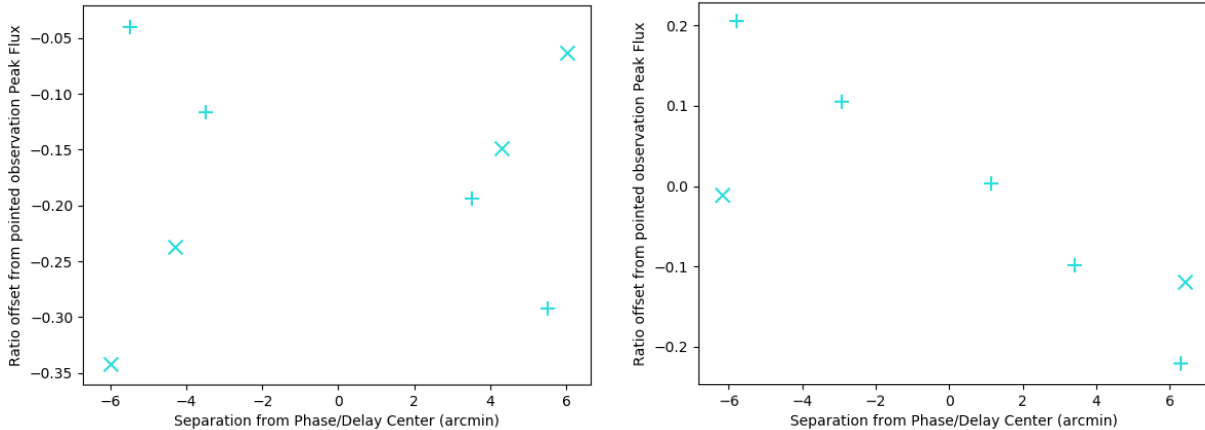


Figure 6: *Left*: Ratio of the difference of peak flux densities after primary beam correction relative to the flux density of a pointed observation of J1915+6548 as a function of distance from the phase/delay center. *Right*: The same as on the left for J0019+7372. The 'x' and '+' symbol indicate points that belong to the same on-the-fly scan row. In both cases only data from RR polarization and spectral window 5 (2.67 GHz) are shown.

integrations. A RA shift by +1.0 integration results in the smallest residual error of the flux densities for the given cases. The corresponding plots, similar to Fig. 6 are shown in Fig. 7. This one integration shift corresponds to an aggregate antenna pointing offset of one integration ahead in time compared to the delay center. This corresponds to a shift in RA direction by 0.06° and 0.0877° for J1915+6548 and J0019+7327 respectively, due to the difference in declination. The variability in peak flux density reduced to a range of $\pm 3.5\text{--}5.0\%$ and is mostly symmetric around the center of the primary beam. From this it appears the antennas are offset by a larger fraction than what is expected from where the antennas are pointed during an OTF row.

Independently, during imaging tests, Urvashi Rao found that spectral indices are inconsistent with simulations when applying wideband-widefield imaging algorithm to VLASS1.1 data. After applying a similar fixvis shift to the visibility data the resulting spectral indices are much closer to what is expected. Fig. 8 illustrates this effect. In this case a VLASS1.1 dataset is used that contains a calibrator, J1448-1620, which was observed during the 2018 BnA configuration (February 2018). Multiple fields were combined from a single row, where the source transits the beam at pointing 18956.7, when it gets closest to the line traced by the OTF scan row. This is marked by the vertical dashed line in the Figures. Each pointing has two integrations, imaged separately. The best result is again obtained when shifting the primary beam by one integration into the future, consistent with the findings above. In addition, some oscillation feature is found for the spectral index when moving away from the center of the primary beam.

To further investigate this pointing offset, dedicated test data was obtained at the be-

Table 1: Corresponding field numbers and distances from the corresponding phase/delay center that were imaged for evaluation of the primary beam correction. The sign in distance indicates the side of the phase/delay center the object was located, a '-' indicates that the right ascension of the source was smaller than the right ascension of the phase center.

Source	field #	Distance (')
J1915+6548	4696	6.03
	4697	4.30
	4698	-4.29
	4699	-6.00
	5080	-5.47
	5081	-3.50
	5082	3.51
	5083	5.50
J0019+7327	11142	-6.18
	11143	6.41
	11199	-5.78
	11200	-2.92
	11201	1.13
	11202	3.42
	11203	6.31

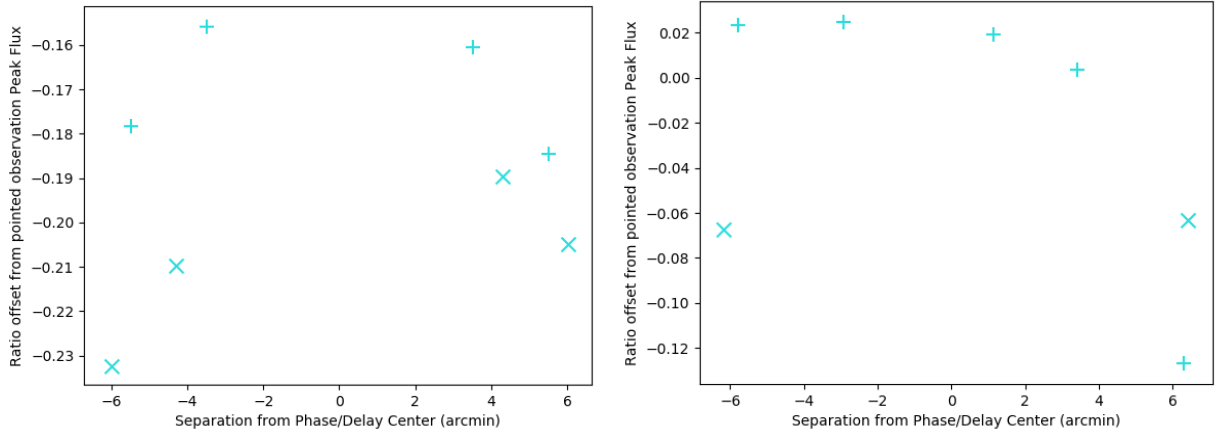


Figure 7: *Left*: Ratio of the difference of peak flux densities after primary beam correction relative to the flux density of a pointed observation of J1915+6548 as a function of distance from the delay center with the visibilities shifted by one integration along the OTF row. *Right*: The same as on the left for J0019+7327. The 'x' and '+' symbol indicate points that belong to the same OTF scan row. In both cases only data from RR polarization and spectral window 5 (2.67 GHz) are shown.

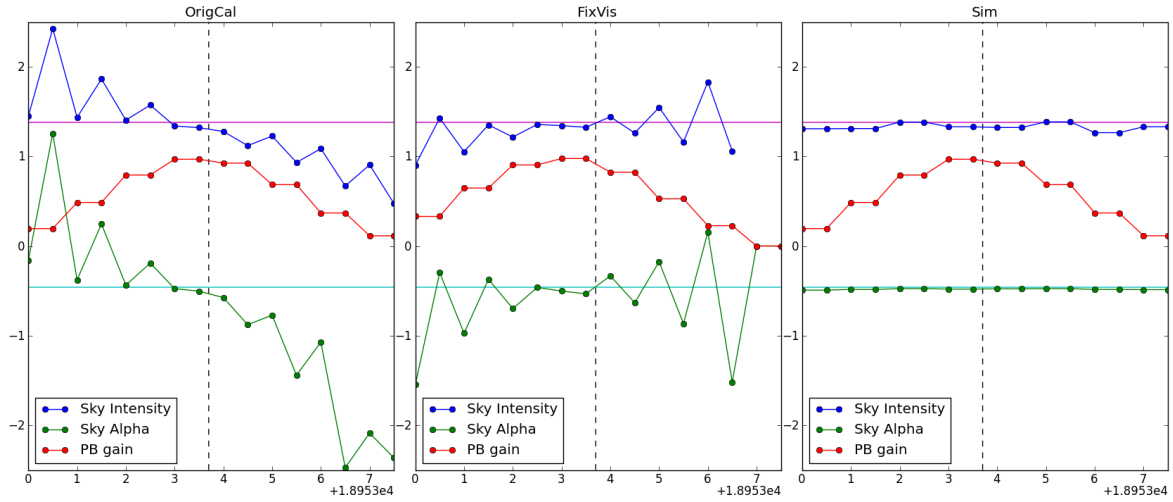


Figure 8: *Left*: Original calibration, *middle*: after applying one integration phase shift, *right*: simulation onto the same VLASS measurement set (to show accuracy achievable if data were perfect). The vertical dashed line indicates when J1448-1620 get closest to the line traced by the OTF scan row. The magenta line is the true intensity of 1.48 Jy. The cyan line is the true spectral index α of -0.46. Each pointing has two integrations, imaged separately. *Image credit: U. Rao*

gining of September 2018 under TSKY0001 by scanning an OTF row with a similar setup to VLASS1.1 over the bright calibrators 3C 147 and 3C 286. Doing so revealed a noticeable pointing offset between antennas that have a new antenna control unit (ACU) and antennas with an old ACU. The new ACU track very well with the delay/phase center location, while the old ACU antennas lead by about 0.9 s (2 integrations). Fig. 9 clearly show this difference. A more detailed analysis by Vivek Dhawan of the Monitoring & Control data stream revealed the azimuth command echo on old ACUs report 0.45-0.5 s ahead of new ACUs. And the elevation command echo on old ACUs report 0.9 s ahead of new ACUs. This is true regardless of az/el rates and this 'feature' is unchanged for the past one year compared to recent data (reaching back to August 29th, 2017) and thus affect all of VLASS1.1 observations. A similar test dataset from June 7th, 2016 does not exhibit this behavior. This issue was introduced with a change that was made in the ACU MIBs in July 2016 and was corrected and put into effect as of September 18th, 2018. At the same time, the pointing table information that is provided with the correlated visibilities and ingested into CASA seems insufficient to diagnose and recognize this offset. Further investigation is needed in order to both fill the pointing table in a useful manner and correctly apply this during imaging in order to account for these differences in pointing going forward in recalibration and imaging of single epoch data products of VLASS1.1 observations.

3.2 Complex Gain Calibration

Here the effect of ionospheric corrections on complex gain calibration is evaluated. The final phase gain calibration tables of the selected representative sample of VLASS1.1 datasets are used to evaluate these three criteria:

1. Phase variability as a function of antenna position, i.e. baseline length to reference antenna.
2. As a function of frequency.
3. As a function of time.
4. As a distribution.

Figs. 10–14 provide visualizations of these four criteria. The standard deviation per spectral window, antenna, and scan is calculated from the pipeline finalphasegaincal table both for calibration performed with and without ionospheric corrections applied. The maximum values within all scans and spectral windows are then plotted against antennas ordered in distance from the core (*top left plots*), where the point with a zero value indicates the reference antenna. Similar plots are provided plotting the maximum value of the distribution of standard deviations against spectral window id, i.e. against frequency from lower to higher (*bottom left plots*) and against scans, i.e. against time (*top right plots*). To provide a full picture of the entire distribution of values a histogram is provided

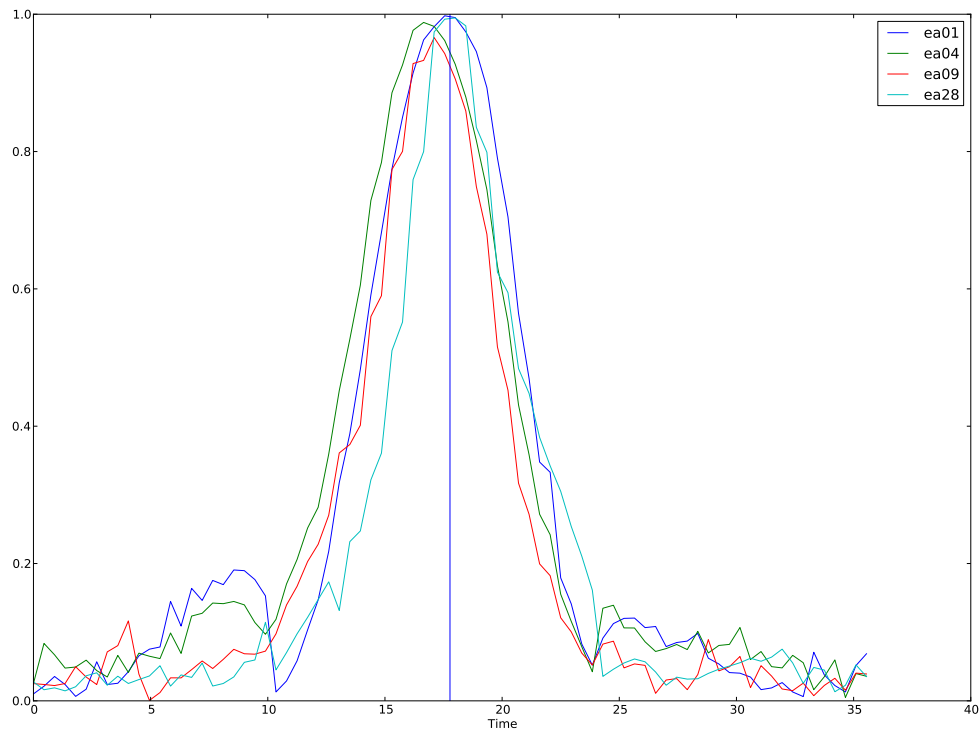


Figure 9: Gain amplitudes with respect to a pointed observation on 3C 147, while scanning a OTF row across 3C147. The vertical line shows the expected peak based on the phase/delay centers reported in the metadata. Antennas ea01 & ea28 have new ACUs, while ea04 & ea09 have old ACUs controlling the antenna pointing.

representing the full spread in phase variations comparing calibration with and without ionospheric correction (TECcorr/noTECcorr).

From these plots we can make the following observations:

- Phase variability increases with baseline length. The magnitude of the effect is independent of ionospheric conditions.
- There is no significant time dependence of phase variability in the selected datasets, with the exception of sb34476823 where an increase in variability of the phases falls into the time period where the projected TEC was dropping at a slow rate. If these phase fluctuations were caused by ionospheric waves during that time, then the coarse input TEC model was not able to capture those changes.
- The projected changes in the TEC shown in Figs. 1 – 5 show a weak relationship with the phase variations. The best matches are found in sb34422762, sb34346984, and sb349202826, where in the first two cases ionospheric corrections have only a small effect on the overall phase variability. However, in the case of sb349202826, applying ionospheric corrections lead to a significant increase in the extreme values of phases, increasing the spread in phase solutions.
- The phase variability is highly dependent on spectral window, where the spectral windows prone to satellite interference are most affected. In many cases the phase variability is higher in spectral windows 2,3 and 11-15.
- There is very little difference in the distribution of phase variabilities comparing calibration with (TECcorr) and without (noTECcorr) ionospheric corrections.

From this we can conclude that the ionosphere in cases of changes in the TEC of > 8 can have an effect on phase stability of calibration. However, it is apparent that the current implementation of applying ionospheric corrections to the data is not adequate to correct for this neither in the low ΔTEC case nor in the high ΔTEC case. The observed changes in phase variability due to suspected ionospheric variability are in the most extreme case of a ΔTEC of ~ 20 the observed maximum phase variability is about 50% higher as compared to the low ΔTEC case.

3.3 Source Positions

To evaluate the effect of ionospheric correction, in particular dispersive delays, 10 square degrees from VLASS1.1.sb34346984.eb34356943.58004.0160307176 were imaged using quick-look imaging pipeline with single epoch continuum image parameters, i.e. using the mosaic gridder both with and without applying ionospheric corrections during calibration. The center coordinates for those fields are: J191707+300000, J192721+67300, J193735+67300, 194749+67300, J195804+67300, J200818+67300, J201832+67300, J202846+67300, J203900+67300,

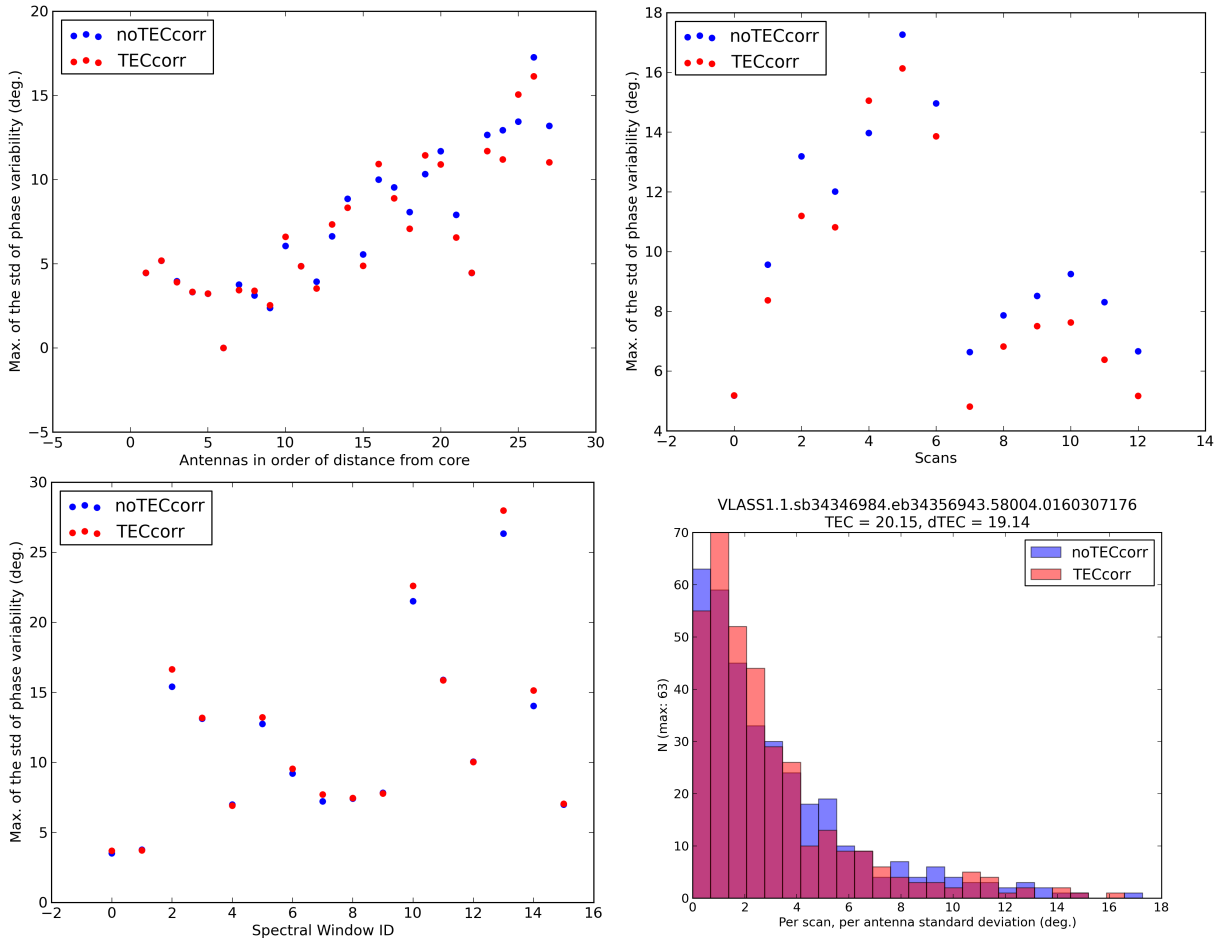


Figure 10: For VLASS1.1.sb34346984.eb34356943.58004.0160307176 values from the pipeline generated finalphasegaincal table are extracted, *top left*: plots the maximum standard deviation of the phase variabilities against antennas in order of distance from the core; *top right*: shows a plot for the maximum standard deviation of the phase variabilities in time (scan numbers are in sequential order and do not represent the true scan numbers within the observation metadata) *bottom left*: plots the maximum standard deviation of phase variabilities against frequency (spectral windows are in sequential order and do not represent the true spectral window numbering from the observation metadata) *bottom right*: shows a histogram of all standard deviation values in each bin of scan, antenna, and spectral window representing the full range of values found in the calibration table. In each plot both the values with and without applying ionospheric corrections during calibration are shown.

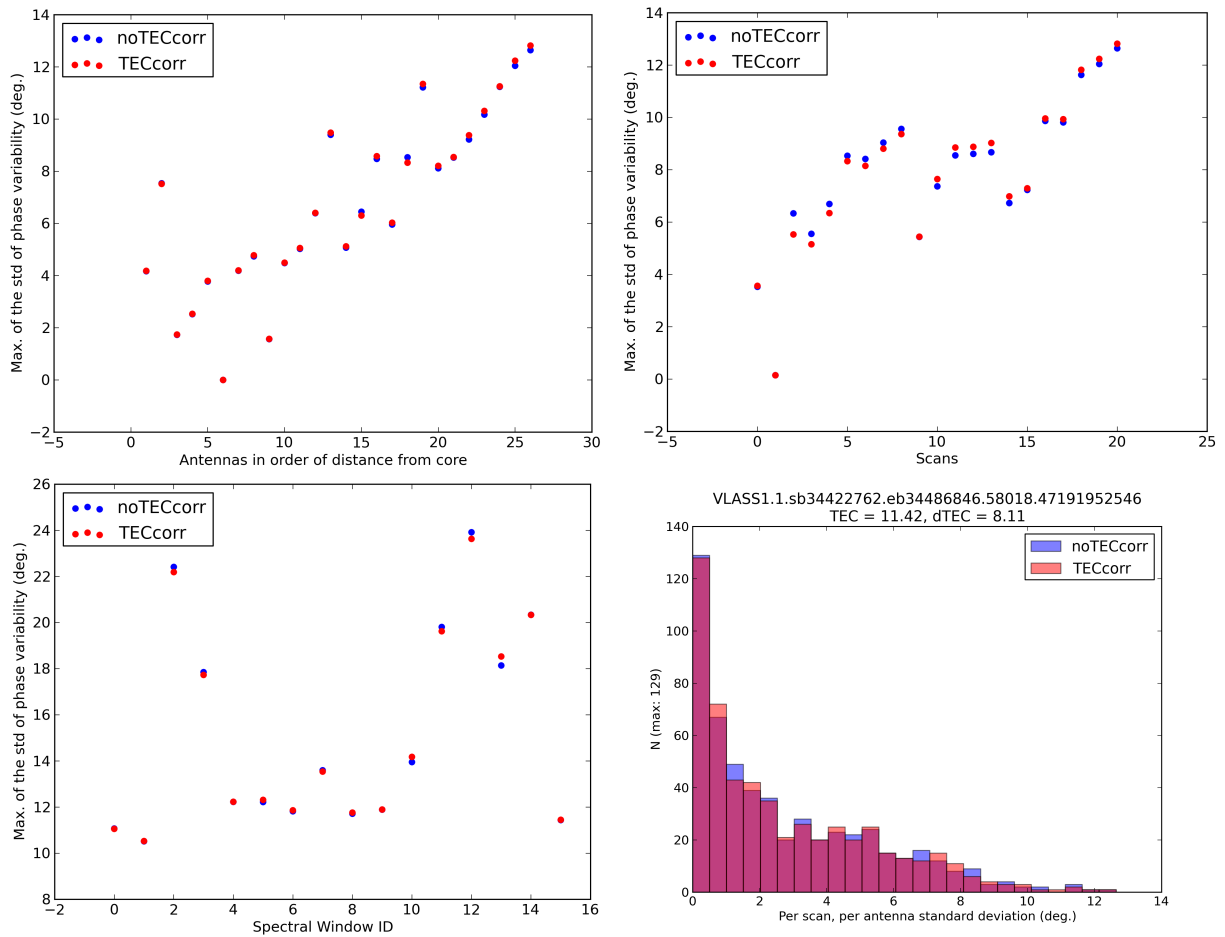


Figure 11: Similar to Fig. 10 for VLASS1.1.sb34422762.eb34486846.58018.47191952546.

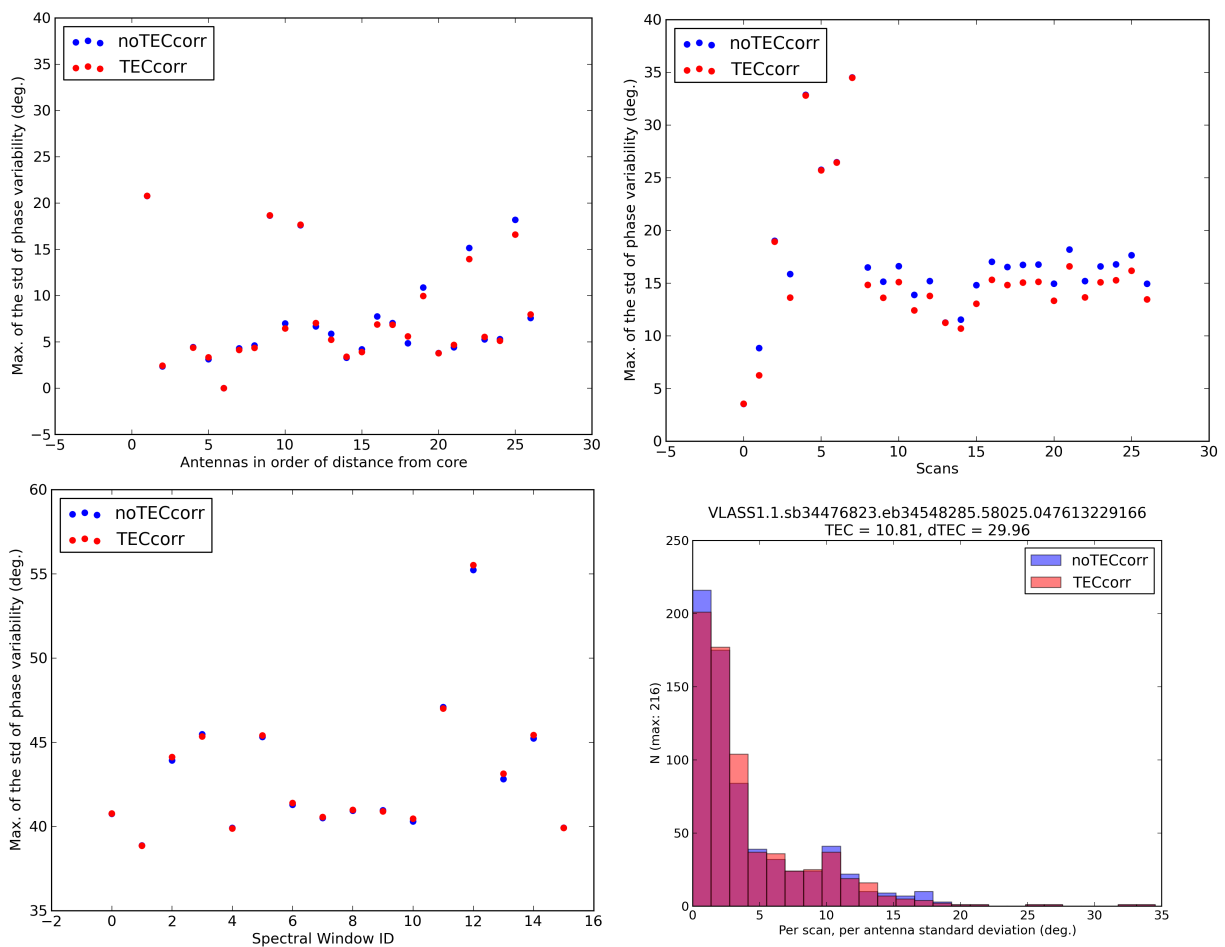


Figure 12: Similar to Fig. 10 for VLASS1.1.sb34476823.eb34548285.58025.047613229166.

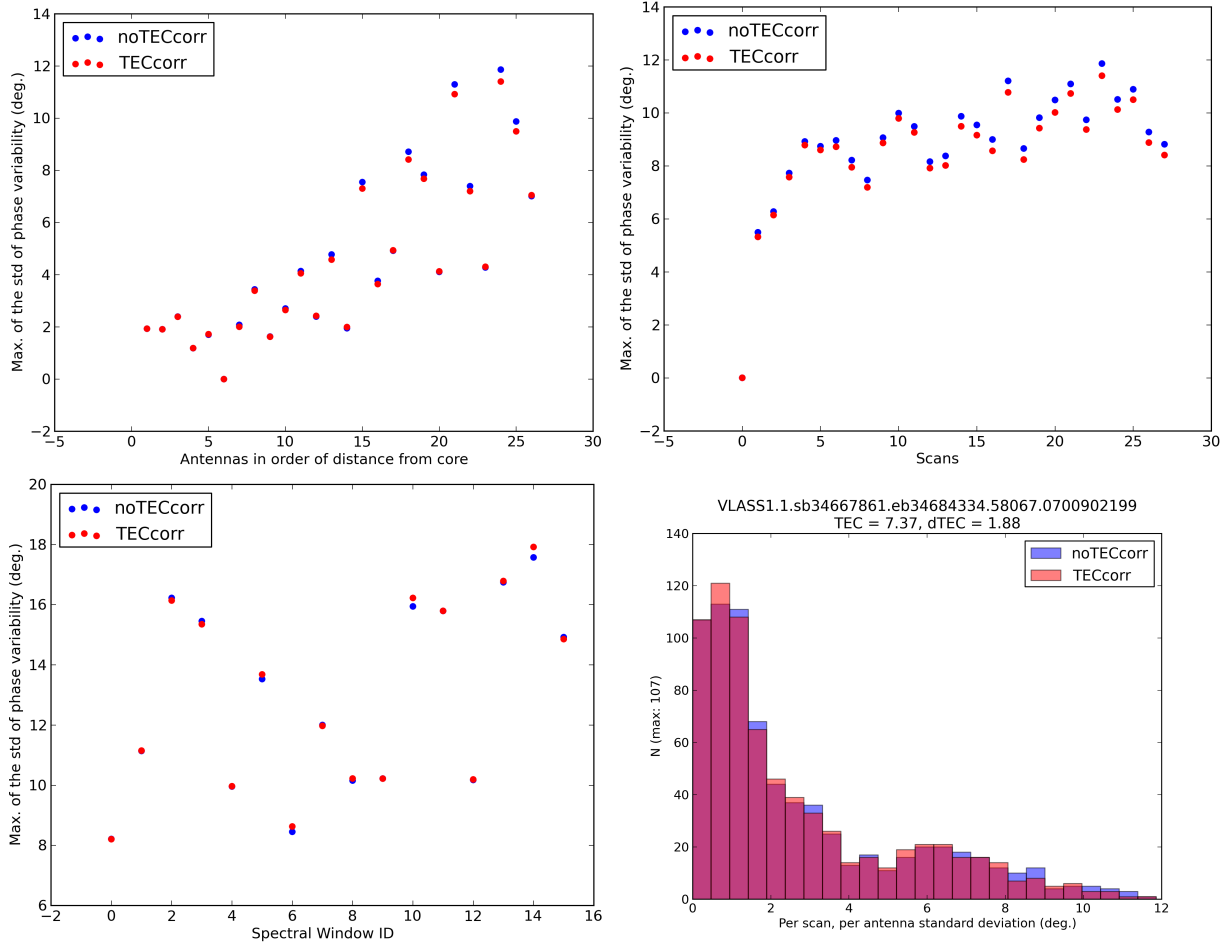


Figure 13: Similar to Fig. 10 for VLASS1.1.sb34667861.eb34684334.58067.0700902199.

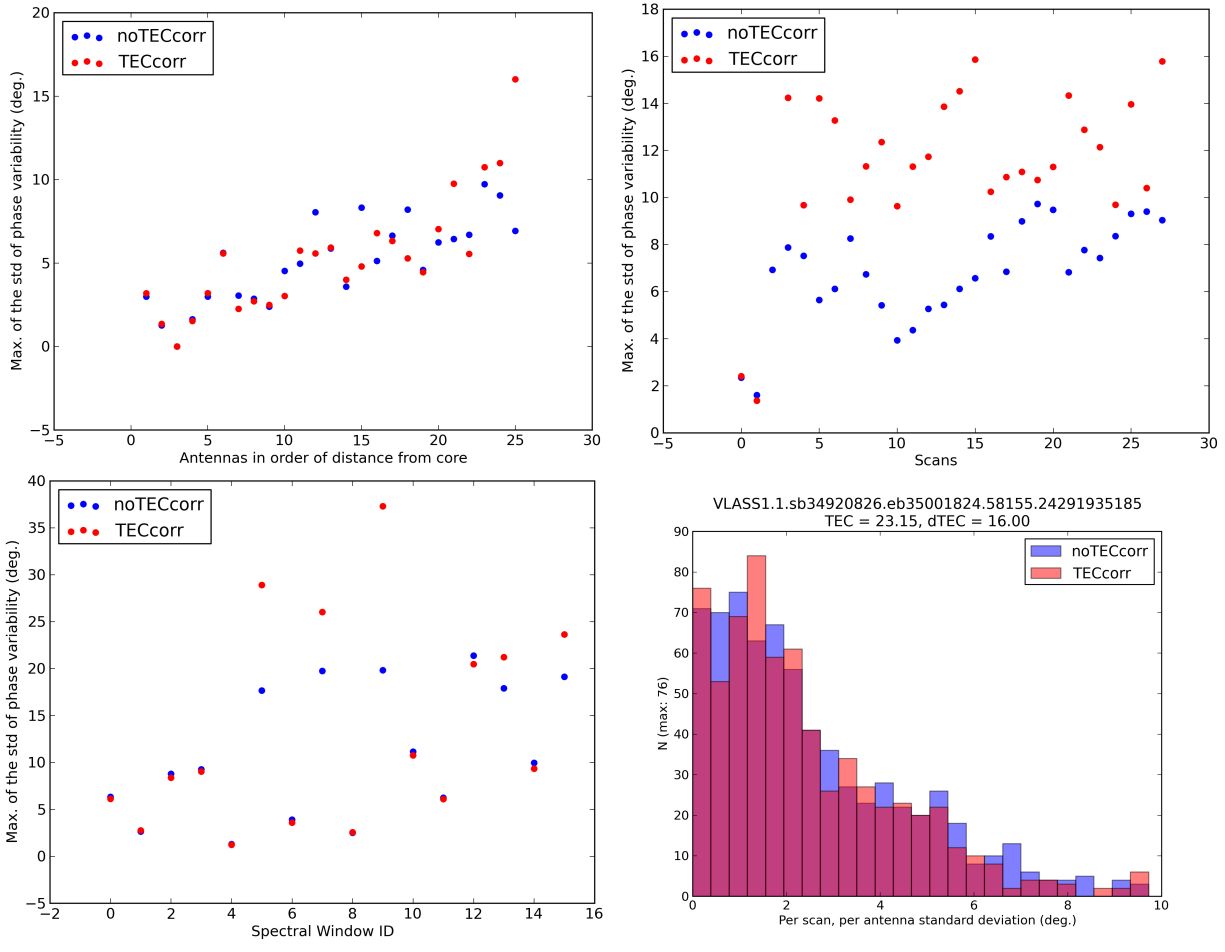


Figure 14: Similar to Fig. 10 for VLASS1.1.sb34920826.eb35001824.58155.24291935185sb34920826.

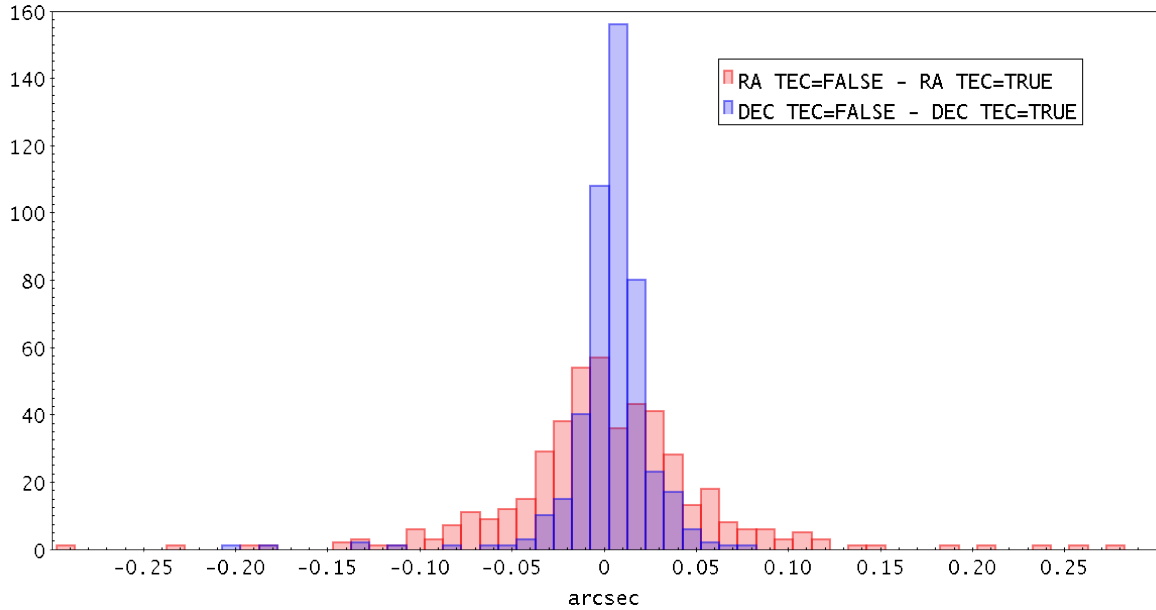


Figure 15: Distribution of position differences between TEC corrected and uncorrected data of matched sources in RA and DEC respectively.

J204604+67300. The pyBDSF⁴ source finder was then used to identify point sources in both fields, which were cross-matched using TOPCAT⁵.

The two catalogs containing each sources from the 10 square degree fields with the two different calibrations are spatially cross-matched with a search radius of 1 arcsec. Fig. 15 and 16 illustrate the distribution of position offsets between TEC corrected and uncorrected images. The offsets are clearly Gaussian distributed and show offset values of <0.12 arcsec, with the majority of much smaller than that. The difference flux density distribution is shown in Fig. 17, which shows a Gaussian like distribution for both the differences in total flux densities as well as the peak flux densities. Thus, concluding that there is no evidence for a difference in source positions when correcting for the ionosphere during calibration as compared to no correction.

In addition, within the 10 square degrees two sources were identified that match sources with VLBI astrometric positions from the radio fundamental catalog⁶. Namely those are, J1947+6750 and J2020+6747 which are not in the VLA calibrator catalog for S-band. The observed position differences are tabulated in Table 2. It is not expected the position accuracies on average much better than $0.1''$, which is consistent with the observations.

⁴<http://www.astron.nl/citt/pybdsf/>

⁵<http://www.star.bris.ac.uk/~mbt/topcat/>

⁶<http://astrogeo.org/rfc/>

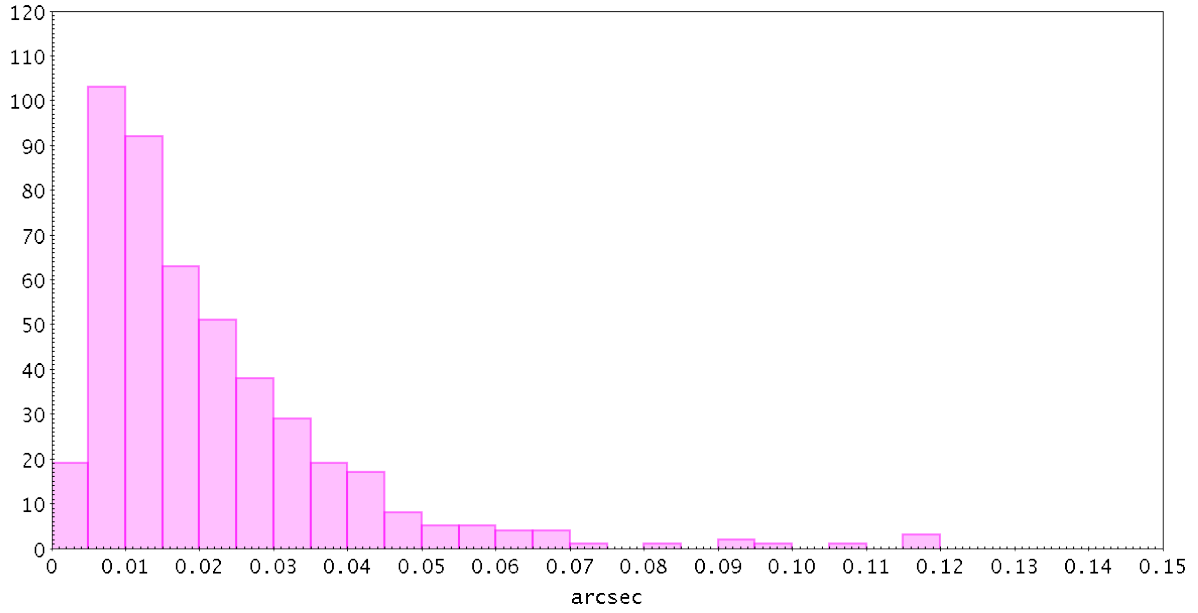


Figure 16: Distribution of relative position differences between TEC corrected and uncorrected data of matched sources.

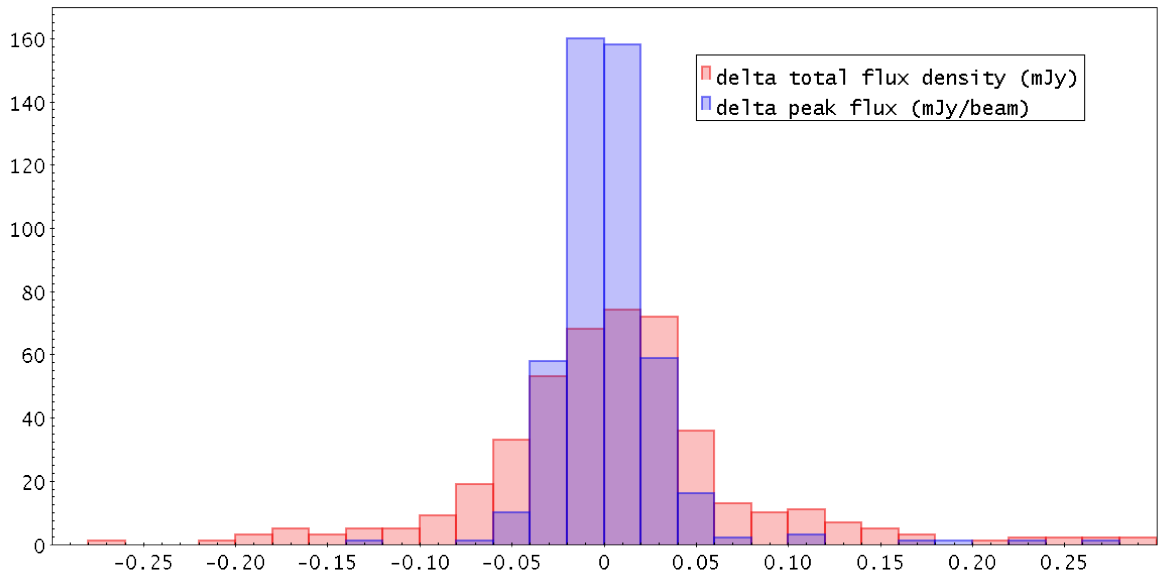


Figure 17: Distribution of differences in total flux density and peak flux between TEC corrected and uncorrected data of matched sources.

Table 2: Comparison of VLBI position offsets with VLASS1.1 derived positions when ionospheric corrections are applied (tecmaps=True) and when they are not applied (tecmaps=False) and the difference of which.

Name	flux	Δ tecmap=False	Δ tecmap=True	difference
J1947+6750	132 mJy	0.34384''	0.34353''	31 mas
J2020+6747	165 mJy	0.70336''	0.57365''	130 mas

3.4 Polarization Properties

To evaluate ionospheric corrections in the context of polarized emission, known calibrators observed within a given VLASS dataset were selected. For each of these sources, OTF fields were selected that contained the calibrator within the full-width at half-maximum of the S-band primary beam ($< 7'$ from the phase/delay center). For each of those fields full-polarization coarse image cubes (one image per spectral window) were produced, which were used to extract polarization properties for each field with and without ionospheric corrections applied during calibration. The properties of each of those objects are listed in Table 3.4.

For each target and imaged field, the median polarization fraction and polarization angle are obtained from the generated image cubes. The difference in linear polarization fraction and angle are calculated comparing calibration with and without ionospheric corrections (uncorrected - corrected). The resulting distributions are shown in Fig. 18. In the case of polarization angles the observed spread in values is primarily located within $\pm 5^\circ$, indicating that the ionospheric corrections are ineffective. In the case of polarization fraction, the ionospheric corrections seem to slightly increase the polarization fraction by about 0.05%. The cause of this is not clear, since ionospheric corrections are only expected to affect delays (dispersive delay correction) and polarization angles (Faraday rotation correction). There is no appreciable difference between the low and high delta TEC datasets.

3.5 Beam Polarization

For the purpose of evaluating the effect of ionospheric corrections on VLASS1.1 OTF fields, we are also able to evaluate the effect of beam polarization for VLASS observations. Similar to the Stokes I primary beam effects discussed in Section 3.1, we can evaluate polarization errors that are introduced by the telescope primary beams and that are not corrected for during imaging.

The calibrator sources found in sb34667861.eb34684334 provide a representative sample of polarized, weakly, and strongly polarized sources. Figs. 19 to 22 show the obtained polarization fractions and polarization angles as a function of distance from the phase/delay center, together with their corresponding on-axis values. Values are plotted for both calibrations with and without ionospheric corrections. In the case of the unpolarized and weakly polarized sources J0017+7327 and J0157+7442, spurious polarization is introduced

Table 3: Bright sources in the selected VLASS1.1 datasets with values obtained from C-array observations in August 2017.

Observation	Source	I@3 GHz (Jy)	PF@3 GHz (%)	PA@3 GHz (deg.)
sb34346984.eb34356943	J1915+6548	0.44	0.2	12.5
	J1933+6540	0.57	1.8	59.0
	J1959+6508	0.27	2.5	-29.7
sb34422762.eb34486846	J0737+6430	0.40	0.03	–
	J0756+6347	0.32	0.08	–
	T0752+6112	0.46	0.05	–
	J0728+5701	0.39	3.6	63.3
sb34476823.eb34548285	J2025+0316	0.34	2.0	0.44
	A2023-0123	0.15	4.3	71.9
	J0022+0014	1.65	0.03	–
	T0032+0136	0.26	0.24	7.91
	J0040+0125	0.12	2.3	-60.6
	C0029-0113	0.25	4.3	-39.0
	T0014-0205	0.22	0.60	-42.0
	C0030-0211	0.31	2.6	44.7
sb34667861.eb34684334	J0157+7442	1.43	0.04	–
	J0019+7327	1.55	0.76	1.29
	J0749+7420	0.61	1.9	-50.7
	J0747+7639	0.44	0.06	–
sb34920826.eb35001824	A0837-3409	0.31	0.93	-43.8

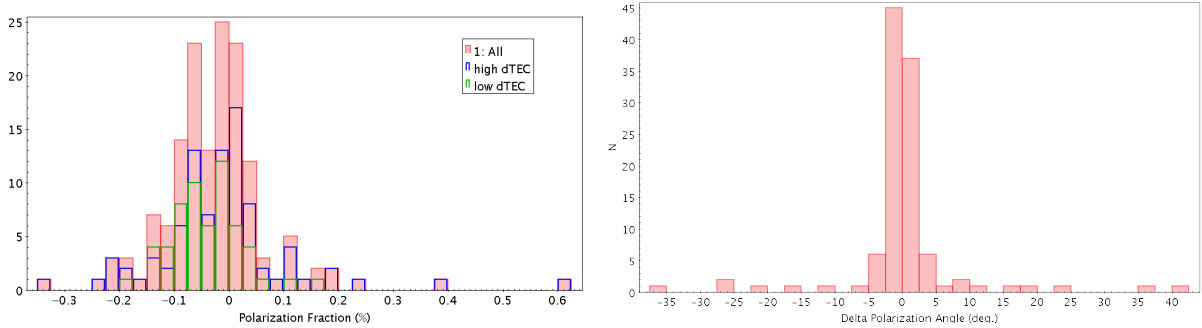


Figure 18: *Left*: Resulting difference in polarization fraction comparing calibration with and without ionospheric corrections applied. The blue lines indicate the subset from the high delta TEC datasets, the green indicates the subset of values from low delta TEC datasets. *Right*: Resulting difference in polarization angles comparing calibration with and without ionospheric corrections applied for polarized sources only.

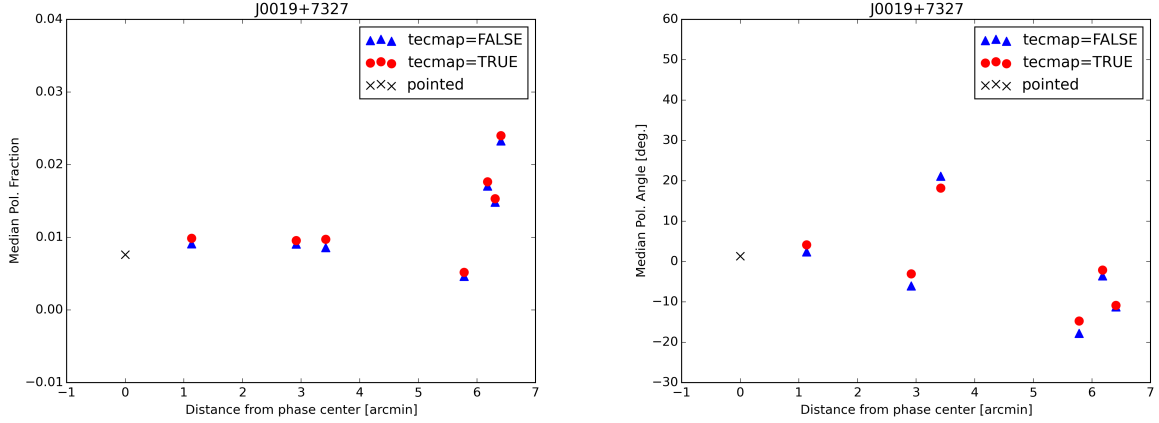


Figure 19: J0019+7327: 3 GHz flux density 1.25 Jy, polarization fraction 0.8%. Left: Polarization fraction as a function of distance from the phase center. Right: Polarization angle as a function of distance from the phase center. In both cases median values are plotted for each field comparing TEC correction applied (red circles) with TEC correction not applied during calibration (blue triangles). For reference the mid-band value at phase center is shown as black cross.

at around 5-6 arcmin from the center of the primary beam, increasing the polarization fraction by up to 3%. Similarly a systematic change in polarization angle is observed. In the case of J0747+7639, which can also be considered unpolarized, the polarization fraction gradually increases to 1.5% of spurious polarization. In the case of the strongly polarized source, the polarization fraction varies by $\pm 30\%$ (0.5% in polarization fraction) and its polarization angle changes rapidly from the nominal value of -50° to -70° by the time the source reaches the half-power point of the primary beam.

Since VLASS1.1 data products will consist of mosaic images that combine multiple fields, the observed variations in single fields is expected to average out. To evaluate this averaging, coarse cube mosaics were computed for each of the four fields above using the mosaic gridded. Fig. 23 compares the derived polarization fractions for the two unpolarized calibrators J0157+7442 and J0747+7639. In the case of J0157+7442 the polarization fraction is observed to be higher by about 0.1% in the OTF mosaic, at the low end of the band the difference is about 0.2%. In the case of J0757+7639 the picture is similar, however there is a regular pattern of spectral windows where the polarization fraction drops to the level of the pointed observation. The third source, J0019+7327, is weakly polarized at around 0.8% linear polarization fraction. In this case, as can be seen in Fig. 24, the OTF mosaic polarization fraction is about 0.2% lower compared to the pointed observation. The observed polarization angle is mostly consistent but shows offsets of up to 5° in polarization angle. The upper end (last four spectral windows) of the band the de-polarization is significantly larger and the polarization angle seems to be not well constrained. The last

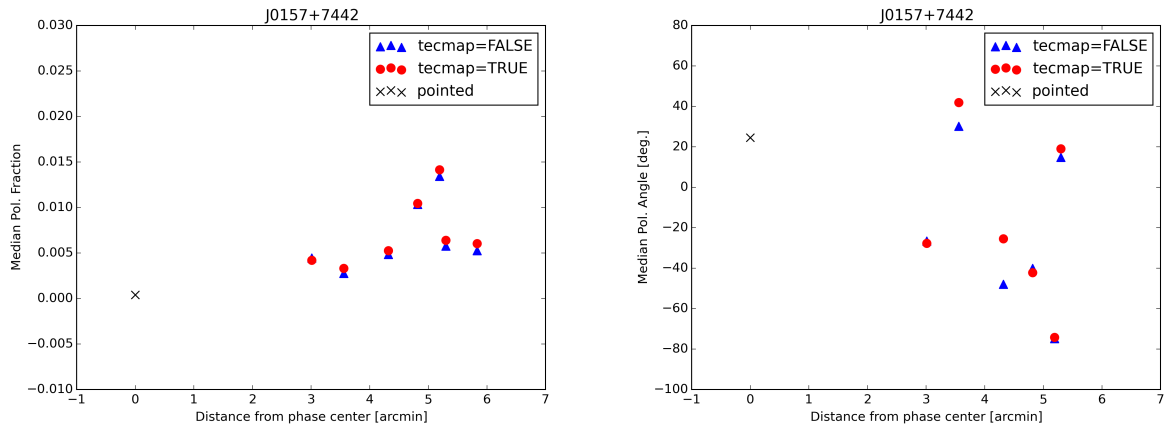


Figure 20: J0157+7442: 3 GHz flux density 1.11 Jy, polarization fraction 0.04%. Similar to Fig. 19.

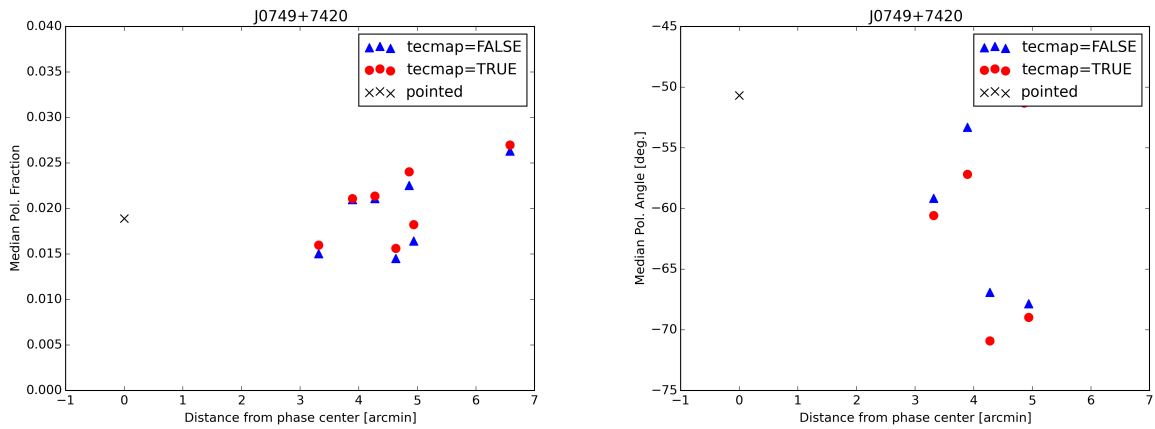


Figure 21: J0749+7420: 3 GHz flux density 0.6 Jy, polarization fraction 1.9%. Similar to Fig. 19.

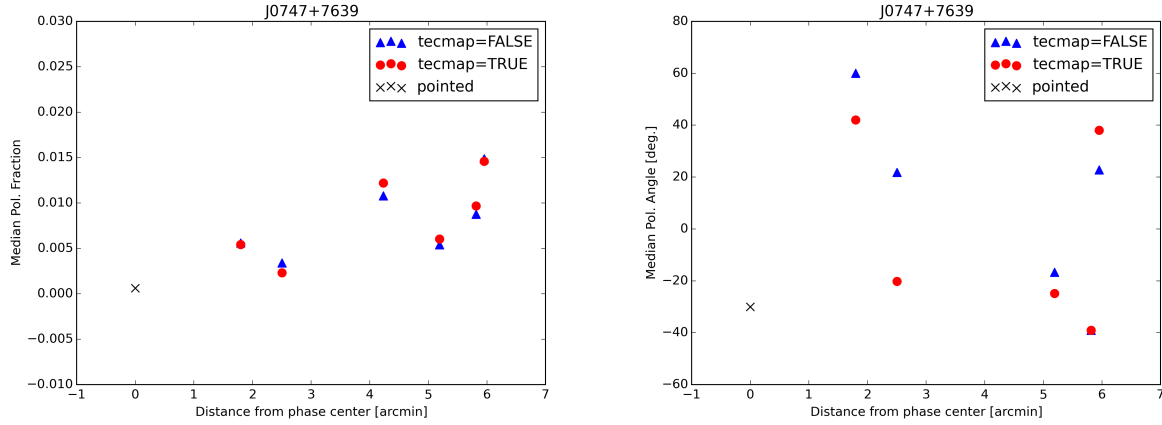


Figure 22: J0747+7639: 3 GHz flux density 0.29 Jy, polarization fraction 0.06%. Similar to Fig. 19.

example is J0749+7420, shown in Fig. 25, which is polarized at the $\sim 2\%$ level. In the OTF mosaic, as compared to the pointed observation, the fractional polarization is dramatically reduced by about 1%. The polarization angles start to deviate significantly above 2.5 GHz increasing the slope of the observed low rotation measure. There are occasional spectral windows that get a correct value.

In summary, it appears that beam polarization plays a significant factor even in the averaged OTF case. The observed differences are at a level inconsistent with the polarization accuracy requirements set for VLASS. Given that the beam polarization effect is direction dependent, no 1D-correction can be applied or a single error can be assigned to measurements derived from VLASS using standard mosaic imaging.

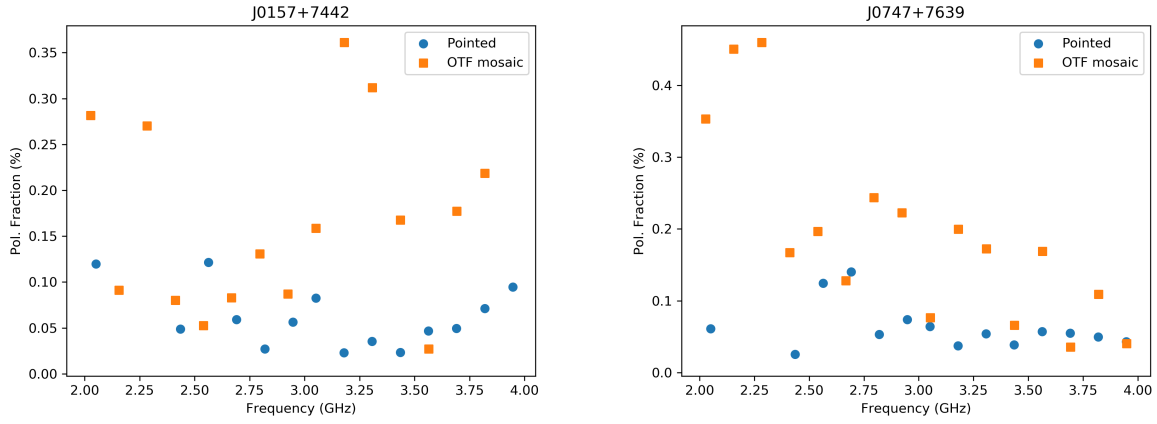


Figure 23: *Left:* Polarization fraction against frequency for J0157+7442 comparing pointed on-axis calibrated observations with OTF mosaic coarse cube results. *Right:* The same as on the left for J0747+7639.

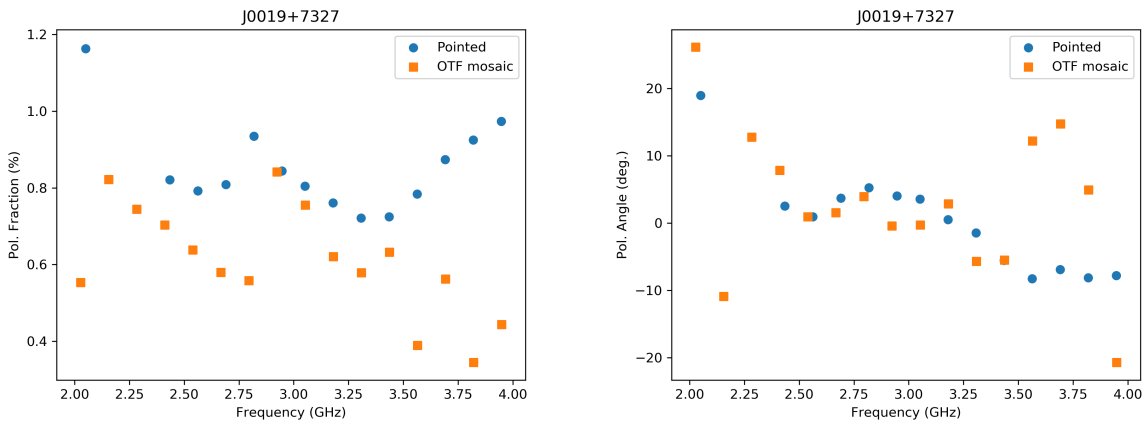


Figure 24: *Left:* Polarization fraction against frequency for J0019+7327 comparing pointed on-axis calibrated observations with OTF mosaic coarse cube results. *Right:* The same as on the left for polarization angle.

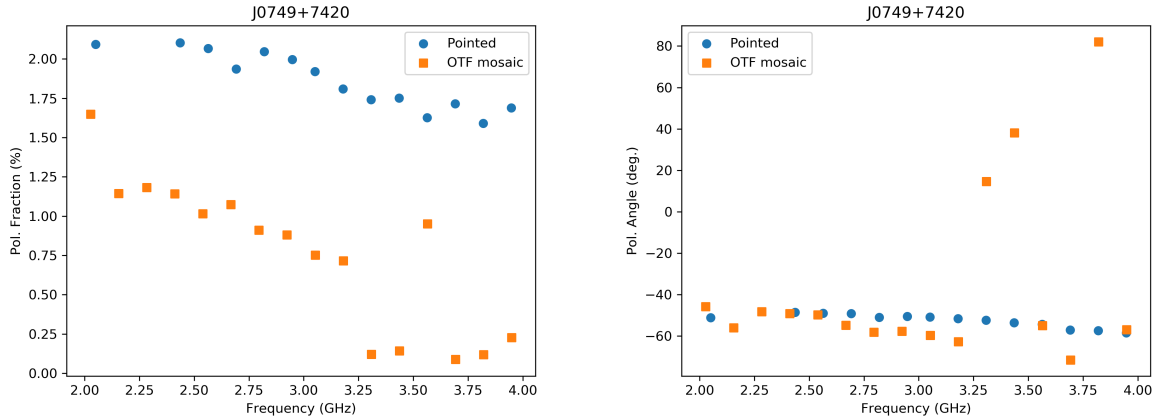


Figure 25: *Left*: Polarization fraction against frequency for J0749+7420 comparing pointed on-axis calibrated observations with OTF mosaic coarse cube results. *Right*: The same as on the left for polarization angle.

4 Summary & Conclusions

- An antenna tracking offset was found, affecting flux densities and spectral indices of VLASS1.1 data products. Antennas with new ACUs appear to track correctly in OTF mode, while old ACU antennas appear to be offset by a constant amount, causing the primary beam correction to not correctly account for beam attenuation.
- The effect of ionospheric corrections is small and can in some circumstances even decrease phase stability during calibration. In general, from the representative data analyzed here the largest influence of the ionosphere on phase stability is estimated to be a 50% increase as compared to a quiet ionosphere.
- There is no noticeable effect beyond statistical errors that applying ionospheric corrections during calibration affects source positions and derived flux densities. This is expected at S-band where effects from dispersive delay are small and which was evaluated in more detail in VLASS memo #5.
- The current ionospheric corrections available through standard IONEX data products and applied using CASA are not adequate to reliably correct for errors introduced by the ionosphere at S-band. Application of such products could even potentially degrade the calibration like in the case of VLASS1.1.sb34920826.eb35001824.58155.24291935185. Significant research & development effort would have to be spent to address ionospheric corrections in the VLASS case. Given the influence of the ionosphere has been benign during VLASS observing and the expectation of low solar activity going forward, it is not clear whether better ionospheric corrections are needed in this

context, especially since tropospheric effects affect VLASS data at similar magnitude (see VLASS memo #10).

- Ionospheric corrections have no statistically significant effect on polarization angles. However, in the case of polarization fractions, ionospheric corrections introduce a slight increase in the polarization fraction on average by about 0.05%, in the worst observed case by about 0.3%. The cause of this increase in polarized fraction is not clear given that ionospheric corrections should only affect source positions and polarization angles.
- Beam polarization dominates polarization errors in comparison to ionospheric effects by orders of magnitude. The polarization properties of a sample of four sources were compared between OTF mosaics and pointed observations. The recorded differences were in particular in the case of a strongly polarized source significant and overall the data would fail VLASS polarization accuracy requirements. It is evident that beam polarization is playing a dominant role in OTF mosaics and is a highly position dependent effect. They are also compounded with a lack of w-projection corrections and the above mentioned antenna tracking issue.

Recommendations:

- The origin of antenna pointing offsets during OTF scans was identified and corrected in the VLA online system going forward. Unfortunately, VLASS1.1 data suffers from this, thus the correct filling and use of the pointing table for imaging purposes has to be investigated prior recalibration and especially imaging for single epoch products of VLASS1.1.
- Better ionospheric models are needed that reflect changes in the ionosphere occurring on short timescales and small spatial scales. In order to do this it might be necessary to deploy a grid of dual-channel GPS receivers to augment models with high time-resolution information that feed into generating corrections to be applied during calibration. Significant research & development is needed in this area that would particularly benefit < 1 GHz and L-band observations, but could also improve calibration for S-band observing, especially during bad ionospheric conditions. Given that this would require significant effort and the so far minimal impact of ionospheric conditions on VLASS observing, it is suggested to defer this item and carry this forward at low or medium priority for VLASS.
- Every VLASS1.1 calibration should include plots that provide information on the ionospheric conditions during the observation, but not apply any ionospheric corrections at this point. Plots and values similar to those shown in Section 2 would be sufficient.
- It is highly recommended to investigate the cause for increased polarization fractions when applying ionospheric corrections for any dataset.

- To meet polarization accuracy requirements set for VLASS, the effect of beam polarization on OTF mosaics has to be characterized and evaluated. While here a first step was taken toward characterization, the next step has to involve the generation of frequency and parallactic angle dependent Stokes Q/U primary beam maps that can be used to correct coarse cube OTF mosaics in order to verify whether such an approach would meet VLASS polarization requirements. This will require data that is unaffected by antenna pointing offsets and takes w-projection effects into account. If this approach of Q/U primary beam correction is determined to not meet VLASS polarization requirements, then a variation of Full Müller matrix imaging would seem unavoidable. If this approach works, further implementation steps can be taken toward applying this correction during VLASS coarse cube imaging.

Revision History

Revision	Date	Author(s)	Description
1.0	2018-10-03	Frank Schinzel	Original